Optical tracking of acoustic radiation force impulse-induced dynamics in a tissue-mimicking phantom

Richard R. Bouchard,[a] Mark L. Palmeri, Gianmarco F. Pinton, and Gregg E. Trahey
Department of Biomedical Engineering, Duke University, Box 90281, Durham, North Carolina 27708

Jason E. Streeter and Paul A. Dayton
Joint Department of Biomedical Engineering, University of North Carolina at Chapel Hill and North Carolina State University, Box 7575, Chapel Hill, North Carolina 27599

(Received 22 December 2008; revised 20 August 2009; accepted 26 August 2009)

Optical tracking was utilized to investigate the acoustic radiation force impulse (ARFI)-induced response, generated by a 5-MHz piston transducer, in a translucent tissue-mimicking phantom. Suspended 10-μm microspheres were tracked axially and laterally at multiple locations throughout the field of view of an optical microscope with 0.5-μm displacement resolution, in both dimensions, and at frame rates of up to 36 kHz. Induced dynamics were successfully captured before, during, and after the ARFI excitation at depths of up to 4.8 mm from the phantom's proximal boundary. Results are presented for tracked axial and lateral displacements resulting from on-axis and off-axis (i.e., shear wave) acquisitions; these results are compared to matched finite element method modeling and independent ultrasonically based empirical results and yielded reasonable agreement in most cases. A shear wave reflection, generated by the proximal boundary, consistently produced an artifact in tracked displacement data later in time (i.e., after the initial ARFI-induced displacement peak). This tracking method provides high-frame-rate, two-dimensional tracking data and thus could prove useful in the investigation of complex ARFI-induced dynamics in controlled experimental settings. © *2009 Acoustical Society of America.* [DOI: 10.1121/1.3238235]

PACS number(s): 43.80.Jz, 43.25.Qp, 43.25.Zx [TDM] Pages: 2733–2745

I. INTRODUCTION

Tissue elasticity imaging is a growing field[1–12] in medical diagnostic imaging whereby underlying mechanical properties of a tissue are gleaned from its mechanical response to an applied force. This response is generally tracked with ultrasound-based displacement estimators, which tend to be unidimensional and often suffer from undesirable sampling limitations. With the imaging of heterogeneous tissues with increasingly complex boundary conditions,[12–15] this induced dynamic response will likewise become more complex (e.g., shear wave anisotropy and plate wave propagation). Consequently, a tracking option with greater spatial and temporal sampling ability could offer valuable insight into these complex dynamics. We propose a novel tracking method that utilizes optical tracking, which is able to track with a high frame rate in two dimensions and is not corrupted by previously transmitted acoustic pulses. These optical tracking data, which were obtained in a tissue-mimicking phantom, are compared to finite element method (FEM) modeling results to further corroborate previously validated simulation results as well as offer corroboration to model elements currently without experimental validation (i.e., lateral displacement values and dynamics during a radiation force excitation).[16] Given the relative closeness (3.3–4.8 mm) of the phantom's most proximal boundary to the region of interest (ROI), this research is limited to transient effects (within the first 4 ms) that occur before this boundary is able to introduce artifacts to the ROI by way of shear wave propagation. Although penetration depth limitations will likely preclude this optically based method from becoming a clinically viable technique, it could still prove useful in understanding complex acoustic radiation force impulse (ARFI)-induced dynamics (e.g., at interface boundaries) or in further validating current FEM modeling results.

A. Acoustic radiation force

ARF is generated whenever an acoustic wave is either absorbed or scattered by an obstructing object. When this wave and object are assumed planar, this force is proportional to the average energy density of the incident wave and can be expressed as

$$\boldsymbol{F}_{\mathrm{rad}} = A\bar{E}\boldsymbol{d}_r, \tag{1}$$

where A equals the projected area on the object, $\bar{E}$ equals the temporal-average energy density of the incident wave, and $\boldsymbol{d}_r$ represents a drag coefficient.[9,17] This drag coefficient has two orthogonal components: the real component represents the force contribution in the direction of incident wave propagation and the imaginary component represents the contribution in the transverse direction. The drag coefficient is defined per unit energy density as

$$\boldsymbol{d}_r = A^{-1}\left(\Pi_a + \Pi_s - \int \gamma \cos\,\theta dA\right) - iA^{-1}\int \gamma \sin\,\theta dA, \tag{2}$$

[a]Author to whom correspondence should be addressed. Electronic mail: rrb@duke.edu

where Π_a and Π_s are the total powers absorbed and scattered, respectively, and γ is the scattered intensity, all per unit incident intensity, while θ is the scattering angle. In the case of many soft tissues and tissue-mimicking phantoms, where the predominant attenuation mechanism is absorption,[18] Eq. (1), which now represents a body force in the direction of incident wave propagation, can be simplified to

$$\boldsymbol{F}_{\mathrm{rad}} = \frac{2\alpha \boldsymbol{I}_{\mathrm{ta}}}{c}, \tag{3}$$

where α equals the absorption coefficient of the medium, $\boldsymbol{I}_{\mathrm{ta}}$ equals the temporal-average beam intensity, and c equals the speed of sound through the medium.[19,20]

When ARF is generated in an elastic solid, displacement is induced within the region of ultrasonic beam propagation; the initial magnitude of this displacement depends on the spatial variation in attenuation and intensity [as indicated by Eq. (3)] throughout this region. Along with this localized displacement, a dynamic ARF excitation produces shear waves, which travel in the transverse direction.[6] In a linear, isotropic, elastic medium, the speed of these shear waves can be expressed as

$$c_T = \sqrt{\frac{\mu}{\rho}} = \sqrt{\frac{E}{2(1+\nu)\rho}}, \tag{4}$$

where μ equals the shear modulus, ρ equals the density of the propagation medium, E is the Young's modulus, and ν is the Poisson's ratio.[21] Typical shear wave velocities in soft tissue range from 1 to 5 m/s.[22]

B. ARF-based tissue elasticity imaging

In the field of tissue elasticity imaging, induced tissue motion resulting from an applied force is analyzed. This force can be static or dynamic and can be applied externally or internally to the human body.[23] The research contained herein is concerned with the specific case when a dynamic force, of relatively short duration (<1 ms), is applied to (or just adjacent to) an internal ROI. An impulsive ARF, or "ARFI" as it will be referred to, is an effective way to create this transient, internal mechanical excitation. Significant research has been conducted on the use of an ARFI excitation for the purpose of tissue elasticity imaging. Current research initiatives have tended to focus on this transient response at the location of the ARFI application ("on-axis")[1–4] or at a lateral location outside of the excitation volume ("off-axis").[5–7] For the purpose of tissue characterization, the magnitude of the on-axis displacement is often inversely proportional to a tissue's mechanical stiffness[24] while the phase velocity of the transversely traveling wave (i.e., shear wave) created by the off-axis displacement is reflective of a tissue's shear modulus [Eq. (4)].[5,9]

C. Current tracking of ARF-induced dynamics

1. Ultrasonically based techniques

Displacement tracking of ARF-induced dynamics is typically achieved through the application of time-delay estimators on radiofrequency (RF) pulse-echo data. Pulse-echo, or "tracking," pulses are transmitted successively at a single lateral beam position to obtain displacement estimates through time for that location; this scheme is then translated laterally to obtain a two-dimensional field of view (FOV). Although this conventional technique can yield sub-micron displacement estimates in the axial dimension,[25] it is hindered by three fundamental limitations: poor tracking resolution in the lateral dimension, sampling limitations due to interference from previous pulses, and a large effective tracking kernel. First, conventional ultrasonically based lateral tracking yields a displacement estimate variance that is 40(focal distance/aperture width)^2 times worse than that achieved through axial tracking.[26] Second, interference from previous pulses limits both tracking pulse repetition frequency (PRF) and the ability to track during an ARFI excitation. Typically, echo signal from previous pulses (tracking or ARF excitation pulses) must be sufficiently attenuated before another pulse-echo tracking scheme can be initiated. Maximum PRF is limited by the desired depth of field, the duration of the excitation pulse (which can generally be ignored for pulse-echo excitations), and the medium's attenuation and speed of sound. If a point located at a focal depth of 3.8 cm was to be tracked in a tissue-mimicking phantom (i.e., 1540 m/s speed of sound), the highest possible PRF would be just over 20 kHz; this would be assuming no residual, interfering echo signal from propagation deep to this focus, which is unrealistic. In practice, PRFs are usually lower than the example given. In the case of tracking an ARFI-induced response, effects of a previously transmitted ARFI excitation tend to persist even longer, given the increase in pulse length (typically one to two orders of magnitude) over conventional pulse-echo excitations.[27] Consequently, pulse-echo tracking during and immediately following an ARFI excitation is generally not possible. Maleke *et al.*[28] were able to track tissue displacement during a continuous wave, amplitude-modulated ARF excitation for the purpose of harmonic motion imaging. By using a tracking pulse transmit frequency between harmonics of the ARF excitation transmit frequency, they were able to suppress interference from the ARF excitation through the application of a bandpass filter. This technique, however, has not been demonstrated with impulsive excitations. Third, the effective tracking kernel for an ultrasonically based method is disproportionally large in the lateral and elevation dimensions due to the inherent width ($\geq$hundreds of microns) of a beam's point spread function. If the magnitude of induced axial displacement varies throughout these lateral/elevational extents, the estimated displacement will tend to average this profile, which will result in an underestimation of the true peak displacement.[29]

2. Optically based techniques

Although there have been multiple nonultrasonically based tracking techniques employed for the purpose of elasticity imaging,[22,30] few have been able to track the transient dynamics generated from an ARFI excitation. Andreev *et al.*[31] first used a laser to track the ARF-induced shear wave dynamics of a 60–100-μm microsphere embedded in an elastic medium. This technique aligned the focus of a laser

on the microsphere, which was used as a shutter to occlude an opposing, coaxial photodiode. An ARFI excitation from an ultrasonic radiator, mounted in the transverse axis, produced a shear wave in the medium that caused the microsphere to move; the degree of photodiode obstruction was proportional to the microsphere's axial displacement. This technique is able to operate at a substantial depth (10 mm from the proximal boundary) and has good displacement estimation resolution (micrometer-order); yet, it only tracks a single particle in a single, orthogonal dimension and gives an indirect measurement of displacement within a range that is dependent on the radius of the obstructing particle. Bossy *et al.*[32] similarly employed the use of a laser, but they instead measured the decorrelation (within 272×272-μm^2 kernels) of received optical speckle patterns, resulting from transmission through a translucent phantom, to gain an indirect measure of internal phantom dynamics generated by shear wave propagation; no embedded microspheres were necessary with this method. This technique is able to function at a significant depth (20 mm) and provides information regarding optical and shear mechanical properties of the tissue, but it offers limited resolution and frame-rate capabilities (millimeter-order and 2 kHz, respectively), does not provide a direct measure of local displacement, and is unable to discern axial from lateral motion.

Perhaps the most standard use for optical tracking of ARF-induced dynamics has been in the investigation of the force's effect on microbubbles, a common ultrasound contrast agent. Using a microscope and attached camera, Dayton *et al.*[33] were able to observe the behavior of a microbubble aggregate when exposed to an ARF excitation. This work was further expanded by Dayton *et al.*[35] and Palanchon *et al.*[34] when they continued to investigate, with a high-speed camera, the effects of ARF on a single microbubble. The experimental configuration presented in this paper is roughly modeled after the basic setup often employed in microbubble experimentation. Bouchard *et al.*[36] recently utilized a similar experimental configuration to track, in two dimensions, the ARF-induced dynamics on the surface of a tissue-mimicking phantom and catheter-based device; these tracking data were then validated with a conventional ultrasonically based tracking technique. Although Bouchard *et al.* were able to track in two dimensions with sub-micron resolution throughout the complete dynamic response, their experimental setup was strictly limited to superficial tracking. Additionally, they included an extra transducer for ultrasound-based tracking, which was not incorporated into this study.

If one were to employ a translucent medium in an optical tracking study, investigation of induced dynamics would not be limited to superficial regions. In the case when light is transmitted through an opaque medium, its intensity decays in an exponential manner which is characterized by the Lambert–Beer law.[37,38] This decay, which tends to be scattering dominated, increases with increased scatterer density in the medium and increased transmission distance of a photon through the medium. Scattering can also cause a defocusing effect to occur when a region within this opaque medium is viewed through an optical microscope. As the number of scatterers between the objective and the focal plane increases, there is an increased contribution from multiply scattered and off-axis photons, which contributes to a loss of focus and contrast in excessively thick samples.

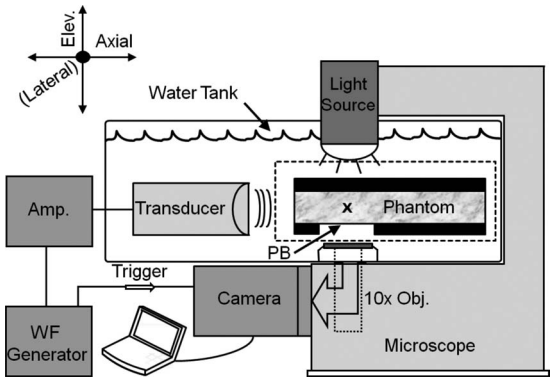

FIG. 1. Experimental setup overview. Dotted box outlines the phantom setup, which is detailed in Fig. 2. "PB" denotes the relative location of the phantom's proximal boundary. "X" indicates transducer/microscope foci. Setup equipment and spacings are not drawn to scale. Presented axes are same as those referenced throughout the paper.

II. METHODS

A. Optical phantom construction

A gelatin-based, translucent, tissue-mimicking phantom was constructed. The gel solution recipe, which was modeled after a formulation by Takegami *et al.*,[39] consisted of the following ingredients (with mass percents given in parentheses): 100 Bloom type-A gelatin (6.8%; Vyse Gelatin Co., Schiller Park, IL), *n*-propanol (3.7%), egg white (35.6%), de-ionized water (53.4%), and 25%-glutaraldehdye (0.5%). Eighteen drops of 10-μm black polystyrene microspheres (Polysciences Inc., Warrington, PA) were added to serve as optical tracking markers. Egg white was included to increase the phantom's acoustic absorption (when compared to gelatin alone) without drastically increasing the optical scattering of the medium. Phantom production was achieved through a similar protocol as that outlined by Hall *et al.*[40] The phantom was initially cast in a 10 cm (diameter) $\times$ 2.5 cm (height) cylindrical mold with acoustic windows on both ends to allow for thru-transmission measurements, which yielded speed of sound and acoustic attenuation measurements (using a substitution method[41]) of 1570 m/s and 0.7 dB/cm (at 5 MHz), respectively, for the experimental phantom. The phantom [Fig. 2(a)] was then removed from the mold, sliced to a 15-mm height, and cut along a 5-cm chord to produce a flat surface along the circumferential perimeter.

B. Experimental setup

All experiments were conducted on the equipment setup depicted in Fig. 1. The basic configuration consisted of a microscope and attached high-speed camera with an ARF-generating ultrasound transducer mounted in the transverse axis. The foci of the microscope and transducer were nearly coincident and positioned in the optical phantom, which was supported by a custom acrylic holder in a water tank.

The ultrasound, or "push," transducer (IL0506HP, Valpey Fisher Corp., Hopkinton, MA) is a single-element

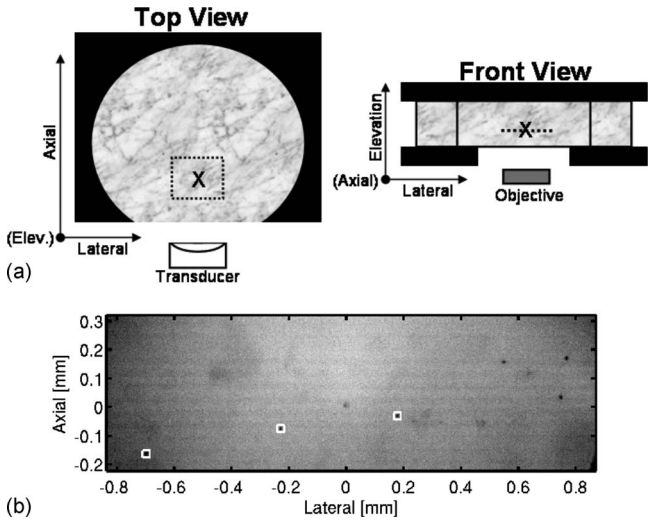

FIG. 2. Phantom setup (a) and microscope FOV example (b). In the right and left phantom setup diagrams, front (side nearest transducer face) and top (upper acrylic plate removed) phantom views are given, respectively. Phantom is denoted by marble shading; acrylic holder, by black shading. Relative positions of the microscope objective and push transducer are identified. Dotted line and box indicate imaging plane and FOV, respectively. "X" indicates approximate transducer/microscope foci. Note cutout in acrylic holder base to allow for optimum microscope visualization. In FOV example diagram, an experimentally utilized (Exp. 6) FOV screen capture (pre-excitation) is given. Six "trackable" microspheres are visible—three in kernel boxes and three (black dots, lateral positions 0.5–0.8 mm) lacking kernel boxes.

piston transducer with a 38-mm focus, 19-mm diameter, 5-MHz center frequency, and a full width at half-maximum (FWHM) beamwidth of 650 μm at the focus (690 μm at 40 mm). The push transducer was mounted to an *XYZ* micropositioning stage (Edmund Optics, Barrington, NJ), with 100-μm precision, for the purpose of precision adjustment. An Olympus IX71 microscope (Olympus America Inc., Melville, NY) fitted with a 10× objective and opposing, coaxial, 100-W halogen illumination source (U-LH100L-3, Olympus America Inc., Melville, NY) was used to gain a magnified visualization of the imaging plane. A high-speed camera (Fastcam SA1, Photron USA Inc., San Diego, CA) was coupled to the microscope to allow for digital frame capture.

To ensure that the foci of the push transducer and microscope were approximately coincident, a needle hydrophone (HNC-0400, Onda Corp., Sunnyvale, CA) with a 400-μm tip diameter was first centered (axially and laterally) within the microscope's FOV and placed in focus (elevationally). With the hydrophone fixed, the push transducer was then adjusted with the micro-positioning stage until the peak amplitude of a repeated 1-cycle burst was placed at the approximate center of the hydrophone in the lateral and elevation dimensions. Due to mechanical limitations on the micropositioning stage, it was not possible to place the spatial intensity peak of the transducer's output at the center of the microscope's FOV in the axial dimension. Instead, a point approximately 2 mm deep to the absolute axial focus was placed at the center of the microscope's FOV. The optical phantom's proximal boundary, which was partially supported by a transparent acrylic holder attached to a second micropositioning stage, was then placed at the coincident transducer/microscope foci. Using the vertical micropositioning stage adjustment, depth into the phantom (relative to the microscope focus) could then be determined based on elevational translation. The flat surface along the circumferential perimeter of the phantom was then positioned 13 mm from the transducer face; this 13-mm water standoff was maintained for all experiments. The phantom was then translated laterally until a reasonably homogeneous region with in-plane microspheres was positioned within the microscope's FOV. The same phantom region was not used throughout experimentation; all utilized phantom regions, however, were within a few millimeters laterally of one another. The push transducer was driven by an arbitrary waveform generator (AWG2021, Tektronix Inc., Wilsonville, OR) and amplified by 55 dB using a RF amplifier (3200LA, Electronic Navigation Industries, Rochester, NY). The ARFI excitation used in this study was measured with a PVDF membrane hydrophone (804–107, Sonic Technologies, Hatboro, PA) to have an *in-situ* intensity ($I_{SPPA.15}$) of 2.5 kW/cm^2 and a mechanical index of 1.8. The output of the waveform generator was synchronized with the high-speed camera to ensure that the video acquisition trigger was coincident with the initiation of ARFI excitation generation. It is important to note that approximately 25 μs of pulse propagation time followed the trigger signal before an ARFI pulse *started* being absorbed at the ROI.

TABLE I. Experimental parameters.

Experiment No.	1	2	3	4	5	6	7
Pulse length (ms)	0.1	0.1	0.2	0.2	0.2	0.4	0.4
Frame rate (kHz)	6.25	10	10	5	36	24	24
Depth (mm)	4.8	4.8	4.8	3.7	3.3	3.3	3.3
FOV offset (mm)	0	0	0	0	0	0	−2:3[a]
No. of trials	1	1	1	3	3	3	1

[a]FOV shifted to six laterally offset locations: 1, 2, 3, −1, −2, and 0 (on-axis) mm; one experimental trial was conducted at each.

C. Experimental protocol

Each experiment was conducted in a similar manner. First, an ARFI excitation, which consisted of a single 5-MHz tone burst of a particular pulse length (given in Table I), was transmitted into the optical phantom at a specific depth from the phantom's proximal boundary. As the push transducer began transmitting the ARFI excitation, the video camera was triggered to capture digital images of the microscope's FOV at a frame rate specified in Table I (the shutter speed was set to the inverse of the frame rate); 8–10 pre-excitation frames were also captured to obtain information regarding the phantom's initial condition. Depending on the experiment, the microscope's FOV was either centered about the approximate location of the push transducer's lateral focus (i.e., on-axis) or laterally offset (but maintaining the same axial/elevation positions) by a specified amount (i.e., off-axis). Specific parameters for each experiment are listed in Table I and depicted in Fig. 3; experiment numbers reflect the actual experimental order. It is important to note that Exp. 8 (presented in Sec. II F) did not involve optical track-

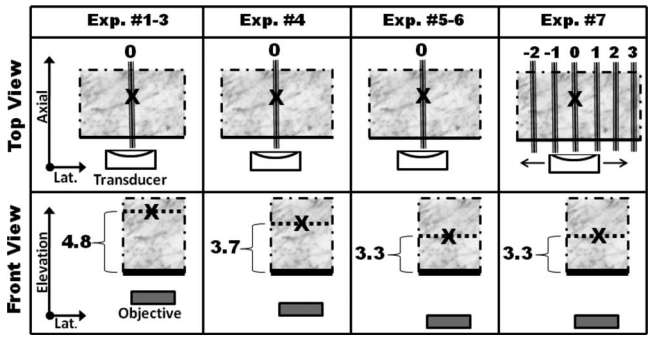

FIG. 3. Transducer/objective positions for all optical experiments. Figure elements (e.g., transducer and objective) and orientations correspond to those depicted above in Fig. 2. Top view provides lateral position of transducer excitation beam (denoted by three vertical lines); front view provides position of microscope focus relative to proximal phantom boundary (denoted by a thick solid line). "X" indicates microscope focus. Entire phantom is not depicted in each figure; only phantom regions nearest transducer/objective face shown. Lateral offsets/depths are given in millimeters. Axes have third dimension label omitted due to space considerations.

ing and thus in not included in the summary table or figure. Camera frame rates and focus depths were limited to 36 kHz and 4.8 mm, respectively, based on approximate points at which light intensity and image contrast became too poor in experimental data to perform reliable tracking. Experimental acquisitions were separated by a minimum of approximately 1 min, during which time the halogen illumination source was turned off, to mitigate phantom heating. Using a digital temperature probe (51-II, Fluke Corporation, Everett, WA), a peak temperature increase of 0.4 °C was measured over 10 s in the phantom due to the illumination source.

The number of trials for each experiment indicates the number of times the experiment was repeated. In the case of Exp. 7, the experiment was conducted once at each FOV offset. To effectively change the microscope's FOV relative to the push transducer's focus, the microscope and phantom were kept fixed while the transducer was precision-translated laterally (depicted in the upper, right-most image in Fig. 3). The transducer was first translated to the five off-axis locations before finally being returned to its approximate original position.

D. Data processing

Displacement tracking was achieved by manually selecting the centers of all in-focus microspheres (typically 1–6) within the microscope's FOV [Fig. 2(b)] and automatically enclosing each in 24×24-μm^2 tracking kernels. Tracking kernels were then translated within a limited radius at each time step, and a correlation coefficient (CCoef), relative to a reference kernel taken from a pre-excitation frame, was calculated for each translation step; the translation corresponding with the highest CCoef for each frame was deemed the most accurate displacement estimate. The post-magnification pixel separation for digitized images was measured with a calibrated reticle slide to be 2 μm; two-dimensional linear interpolation was utilized to allow for sub-sample shifts of 0.5 μm, a reasonable limit given the average signal-to-noise ratio (SNR) encountered in the video data during experimentation.

Shear wave and lateral displacement wave velocity estimates were obtained by implementing a time-of-flight method, the lateral time-to-peak (TTP) algorithm,[42] on displacement data acquired from kernels outside of the ARFI excitation volume (i.e., off-axis). In general, the time-to-peak displacement (TTPD) for a specific kernel was plotted as a function of its lateral distance from the excitation center. A linear regression fit was then performed on these data to yield a wave velocity estimate (obtained from the fit's inverse slope). The square of a fit's correlation coefficient was calculated to indicate its degree of linearity, with $r^2=1$ indicating perfectly linear data. When TTPD values were calculated for lateral displacement data, a running average was applied through time with a 167-μs kernel length. The same filter was applied to axial displacement data prior to differentiating for the purpose of obtaining kernel velocity estimates in Exp. 5.

In an effort to concisely quantify the tracking quality of displacement data, three metrics related to the CCoef are presented in Sec. III with all tracked data: lowest (among all kernels represented in the figure) average CCoef, highest standard deviation, and lowest CCoef value achieved—all through time for a single kernel but not necessarily the same kernel. These parameters, which are listed in an array ($CCoef_{worst}=[\min(avg),\max(std),\min(value)]$), are meant to give a worst case depiction. Typical per-frame CCoef values were above 0.85 for Exps. 1–5 and above 0.9 for Exps. 6 and 7; CCoef values were always lowest during transmission of the ARFI excitation.

E. FEM modeling

Three-dimensional FEM models of the dynamic response of elastic media to ARFI excitations were used to confirm the underlying physical mechanisms responsible for the experimentally observed dynamics. These models utilized a mesh of 1,175,000 eight-noded, linear cubic elements with 0.1-mm node spacing. The model was performed in three dimensions using quarter-symmetry (about the transducer's axis of symmetry) boundary conditions. The lateral/elevation dimensions of the mesh extended 5 mm from this axis of symmetry while the axial dimension extended 6 cm from the transducer face. Degrees of freedom for the symmetry faces were set for their appropriate symmetry conditions, the "outer" faces were unconstrained, and the bottom and top boundaries were fully constrained. The material was modeled as a linear, isotropic, elastic (i.e., no viscosity) solid with $E=3.4$ kPa, $\nu=0.499$, and $\rho=1.0$ g/cm^3. The Young's modulus value was determined through shear wave velocity data obtained in Exp. 8 (presented in Sec. II F) and Eq. (4), a relationship which was experimentally validated in gelatin-based phantoms.[16]

Simulation of the acoustic intensity associated with the piston utilized in these experiments was performed using FIELD II, a linear acoustics modeling software package.[43,44] The piston (38-mm focus, 19-mm diameter) was simulated in FIELD II using the xdc_concave function with 0.5-mm square mathematical sub-elements. No attenuation was simulated in the water path (0–13 mm), and the effects of nonlinear wave

propagation in the water and reflections at the water/phantom interface were not taken into account in these simulations.

The radiation force field was applied as point loads to individual nodes in the region of excitation. The magnitude of these point loads was determined using Eq. (3), where the intensity was averaged over the adjacent element volume for a given node, and the attenuation was 0.15 dB/cm MHz. Forces were applied for the specified pulse length duration and directed along the Poynting vector as a function of position in the region of excitation. For the on-axis result, simulation parameters were based on Exp. 5; for the off-axis result, they were based on Exp. 7.

The dynamic response of the elastic solid was solved through the balance of linear momentum and using LS-DYNA3D (Livermore Software Technology Corp., Livermore, CA), which implemented an explicit, time-domain, integration method. Single-point quadrature was used with Flanagan–Belytschko integration stiffness form hourglass control to avoid element locking and to reduce numerical artifacts. Two-dimensional linear interpolation was employed on the modeling result to obtain displacement values at the specific lateral/axial kernel positions. To obtain registration between model results and optically tracked data, the experimental FOV center was assumed to be perfectly centered in the lateral/elevation beam dimensions and located 40 mm (i.e., 2 mm deep to the simulated axial focus) from the transducer face in the axial dimension. Pulse propagation time to the ROI was accounted for in the model results. All of these modeling methods have been applied previously to gelatin-based phantoms, as detailed by Palmeri *et al.*[16]

F. Ultrasonically based shear wave velocimetry

A SONOLINE Antares™ ultrasound system with a VF10-5 commercial linear array (Siemens Medical Systems, Ultrasound Group, Issaquah, WA) was used for independent ultrasonically based validation of the shear wave velocity estimate in the phantom. ARFI excitations were generated from and tracked with the linear array probe. Inclusion of egg white solution in the gelatin-based phantom generated enough backscatter to allow for reliable ultrasonically based tracking. From the tracked data, shear wave velocity estimates were obtained with the lateral TTP algorithm, the implementation of which is described in detail by Palmeri *et al.*[42] Shear wave velocity estimates were acquired at three independent regions in the experimental phantom. This protocol will be referred to as Exp. 8.

III. RESULTS

Optical tracking results, which are presented first, focus on three specific aspects: on-axis dynamics (Exps. 1–6), off-axis dynamics (Exp. 7), and proximal boundary effects (Exps. 1–4 and 6). These results are then compared to matched FEM modeling and ultrasonically based shear wave velocimetry (Exp. 8) results.

A. On-axis dynamics

Figure 4 depicts the on-axis dynamic response for Exp. 6 from Table I and Fig. 3. The dynamic responses of six embedded microspheres (each tracked with a single kernel) are presented by identifiably colored traces. Specifics regarding kernel location (relative to the bottom image in Fig. 2), displacement peaks (positive or negative), and TTPD values are presented in Table II.

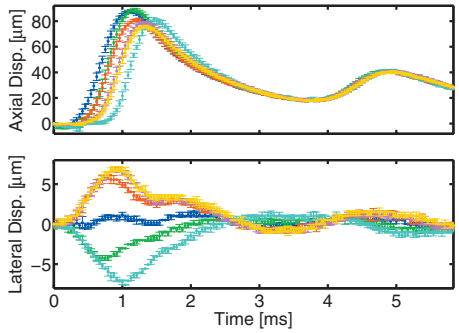

FIG. 4. Tracked axial (above) and lateral (below) displacement induced by 0.4-ms ARFI excitation. Each trace depicts the mean and standard deviation ($N=3$) with dots and error bars, respectively, for a specific tracked kernel at sampled time points (24-kHz frame rate). Corresponding trace colors (blue, green, red, cyan, magenta, and yellow —represented by first letter of respective color name) and coordinates of plotted kernels ($CCoef_{worst}=[0.85,0.05,0.65]$) are presented in Table II. Coordinates for all figures are relative to the FOV center. Time scale commencement for all figures is coincident with the initiation of ARFI excitation transmission. Unless otherwise noted, abscissa and ordinate scales are the same for plots within a given figure and all plotted data are unfiltered.

In the axial displacement plot (above), there are two displacement peaks: one resulting from the initial ARFI excitation (occurring between 1.13–1.46 ms) and one resulting from the proximal boundary shear wave (PBSW) reflection (occurring around 5 ms). In the lateral displacement plot (below), the direction of a kernel's displacement depends on its lateral position relative to the excitation center; a kernel will tend to displace away from the excitation's central axis. Much like the axial displacement plot, there are two peaks in absolute displacement presented in the lateral displacement plot: one resulting from the initial ARFI excitation (occurring between 0.71–1.00 ms) and a subtle one resulting from the PBSW reflection (occurring around 5 ms).

The peak displacement and TTPD values for each kernel are listed in Table II. Peak lateral displacement magnitude and TTPD, in both the axial and lateral dimensions, values tend to increase as a kernel's lateral distance from the excitation center increases. A notable exception to this trend is the cyan trace, which peaked (in axial and lateral displacement) latest and experienced the greatest lateral displacement despite having a reported absolute lateral distance (0.70 mm)

TABLE II. Exp. 6 on-axis (Fig. 4) kernel parameters.

Trace color	B	G	R	C	M	Y
Axial pos. (mm)	−0.04	−0.08	0.15	−0.17	0.03	0.17
Lateral pos. (mm)	0.18	−0.23	0.55	−0.70	0.75	0.77
Peak ax. disp. (μm)	87.9	88.9	81.0	80.5	78.6	75.9
Axial TTPD (ms)	1.13	1.17	1.21	1.46	1.29	1.33
Peak lat. disp. (μm)	0.9[a]	−4.2	5.6	−7.2	6.6	6.8
Lateral TTPD (ms)	0.96[a]	0.71	0.79	1.00	0.92	0.92

[a]Search region limited to first 1.25 ms.

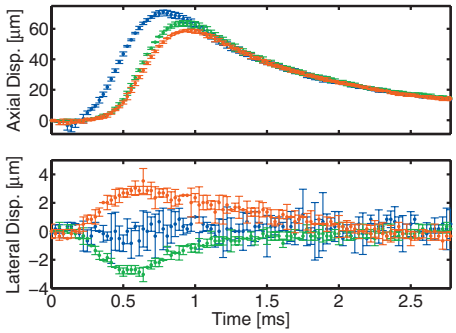

FIG. 5. Tracked (36 kHz) axial (above) and lateral (below) displacement induced by 0.2-ms ARFI excitation. Corresponding trace colors and coordinates of plotted kernels ($CCoef_{worst}$=[0.73,0.06,0.46]) are presented in Table III. Both plots are truncated to allow for better visualization of early-time dynamics; windowing removed PBSW reflection peak (occurring around 5 ms). All other plotting conventions are the same as those used in Fig. 4.

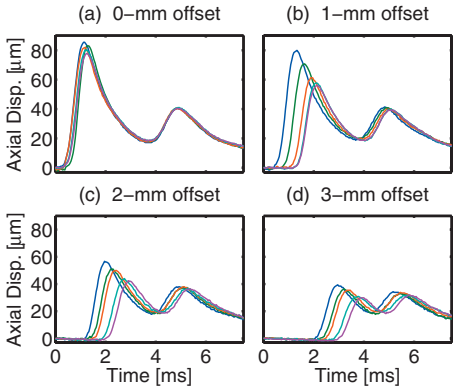

FIG. 6. Tracked (24 kHz) axial displacement resulting from 0.4-ms ARFI excitation centered relative to FOV of on-axis plot (a). FOVs for the other three plots [(b)–(d)] are increasingly offset laterally (1, 2, and 3 mm, respectively). Each trace represents a single tracked kernel ($CCoef_{worst}$=[0.86,0.03,0.76]; same for Fig. 7). Corresponding trace colors and kernel coordinates are presented in Table IV.

that was closer than the magenta and yellow kernels (with 0.75 and 0.77 mm lateral distances, respectively).

Figure 5 depicts the on-axis dynamic response for Exp. 5. The dynamic responses of three embedded microspheres are represented by identifiably colored traces. Similar kernel parameters to those offered for Exp. 6, with the notable inclusion of peak axial velocities and corresponding occurrence times, are presented in Table III.

As in the previous on-axis case, peak lateral displacement and axial/lateral TTPD values increase while peak axial displacement values decrease as a kernel's absolute lateral offset increases. A kernel's peak axial velocity and the corresponding time at which it occurs likewise increase as absolute lateral distance increases. In the axial displacement data (above), the blue kernel experienced a significant decrease in its CCoef, to 0.46, during absorption of the ARFI excitation (around 0.15 ms). This resulted in noticeably increased tracking jitter in its axial displacement plot (blue trace) and what is assumed to be an artifactual, mean negative displacement.

B. Off-axis dynamics

Figures 6 and 7 summarize the off-axis response resulting from Exp. 7 (0–3 mm offsets). Figure 6 presents axial displacements, while Fig. 7 presents lateral displacements at four FOV offsets. Appropriate kernel parameters are presented in Table IV and apply to both figures. In all plots, two displacement peaks occur for each trace. The earlier peak is due to the initial excitation volume displacement or the outgoing shear wave it creates; the later peak is due to the PBSW reflection.

In the on-axis plots [0-mm offset— Figs. 6(a) and 7(b)], similar traits are observed when compared to the previous two on-axis experiments (Exps. 5 and 6). For the most part, kernels with greater lateral offset achieve less axial displacement but greater lateral displacement and axial/lateral TTPD values. Much like the first example presented (Exp. 6), there was one kernel, represented by the green trace, that had lateral displacement and TTPD values that were greater than expected. Additionally, the blue kernel experienced substantial negative lateral displacement (−1.7 μm) despite reportedly being located in the positive lateral region (0.17 mm).

In the off-axis, axial displacement plots [Figs. 6(b)–6(d)], observed behavior is similar to noted on-axis dynamics. Kernels further from the ARFI excitation center achieve a displacement peak that is less in magnitude and occurs later in time. As FOV offset increases, there is a greater amount of time following transmission of the ARFI excitation when no displacement is observed, indicating that the outgoing shear wave has not yet reached those more distal kernels. The PBSW reflection peak in each axial displace-

TABLE III. Exp. 5 on-axis (Fig. 5) kernel parameters.

Trace color	B	G	R
Axial pos. (mm)	−0.13	0.03	0.17
Lateral pos. (mm)	0.04	−0.20	0.50
Peak ax. disp. (μm)	71.0	63.6	58.9
Axial TTPD (ms)	**0.78**	**0.92**	**0.94**
Peak lat. disp. (μm)	−0.3[a]	−2.8	3.0
Lateral TTPD (ms)	**0.47**[a]	**0.56**	**0.61**
Peak ax. velocity (m/s)	0.184	0.174	0.154
Velocity peak time (ms)	0.47	0.61	0.61

[a]Search region limited to first 0.75 ms.

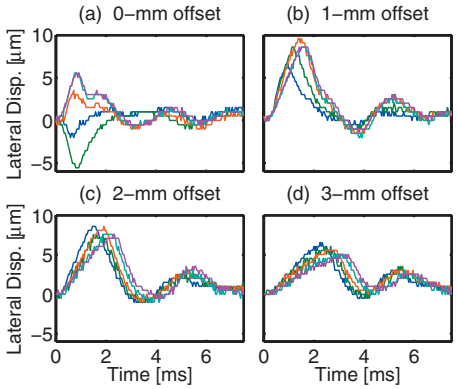

FIG. 7. Tracked (24 kHz) lateral displacement resulting from ARFI excitation centered relative to FOV of on-axis plot (a). Same kernels, FOVs, and plotting conventions are used as those presented in Fig. 6.

TABLE IV. Off-axis (Figs. 6 and 7) kernel parameters,

	(a) 0-mm offset				
Axial pos. (mm)	−0.07	−0.12	0.11	−0.01	0.13
Lateral pos. (mm)	0.17	−0.23	0.55	0.75	0.77
Peak ax. disp. (μm)	85.5	83.0	82.0	80.5	77.9
Axial TTPD (ms)	1.13	1.25	1.17	1.25	1.25
Peak lat. disp. (μm)	−1.7	−5.5	3.0	5.5	5.4
Lateral TTPD (ms)	0.63	0.83	0.71	0.83	0.83
	(b) 1-mm offset				
Axial pos. (mm)	−0.10	−0.05	0.13	0.01	0.15
Lateral pos. (mm)	0.77	1.17	1.55	1.75	1.77
Peak ax. disp. (μm)	79.9	70.8	61.2	57.7	56.2
Axial TTPD (ms)	**1.33**	**1.63**	1.88	**2.08**	2.13
Peak lat. disp. (μm)	6.2	8.4	9.4	8.6	8.6
Lateral TTPD (ms)	**0.92**	**1.17**	1.42	**1.58**	1.58
	(c) 2-mm offset				
Axial pos. (mm)	−0.10	−0.02	−0.06	0.13	0.01
Lateral pos. (mm)	1.77	2.00	2.17	2.54	2.74
Peak ax. disp. (μm)	56.7	51.1	50.1	44.0	42.5
Axial TTPD (ms)	1.96	2.21	**2.42**	2.75	**2.92**
Peak lat. disp. (μm)	8.5	7.3	8.2	7.6	7.3
Lateral TTPD (ms)	1.50	1.58	**1.83**	1.96	**2.33**
	(d) 3-mm offset				
Axial pos. (mm)	−0.10	−0.02	−0.06	0.13	0.01
Lateral pos. (mm)	2.76	2.99	3.17	3.54	3.74
Peak ax. disp. (μm)	39.5	36.4	35.4	30.9	29.9
Axial TTPD (ms)	2.96	3.21	3.33	3.75	3.88
Peak lat. disp. (μm)	6.3	5.7	5.6	4.9	5.1
Lateral TTPD (ms)	2.29	2.38	2.54	3.00	3.08
Trace color	B	G	R	C	M

ment plot occurs around 5 ms. Yet, these TTPD values progressively spread out and corresponding peak displacements attenuate as kernel offset increases. In the on-axis case (a), PBSW reflection peaks are virtually coincident while they are clearly dispersed, with a range of about 1 ms, and sequentially attenuated in the 3-mm offset case (d).

In the off-axis, lateral displacement plots [Figs. 7(b)–7(d)], observed dynamics are more complex than in the axial case. With all kernels in the positive lateral region, lateral displacements were consequently positive in all cases. Additionally, TTPD values increased as kernel offsets increased. Peak lateral displacement values, however, did not simply increase with increasing lateral kernel distance. In the 1-mm offset plot (b), peak displacement begins to increase with increasing kernel distance for the closest three kernels, but then it decreases for the furthest two kernels. The behavior in the 2-mm offset plot (c) is even less clear, with peak displacements tending to oscillate with increasing kernel offset. In the 3-mm offset plot (d), peak displacement tends to decrease with increasing kernel distance. Unlike the off-axis, axial displacement plot, there is no displacement delay with increasing FOV offset. With all three offsets, monotonically increasing lateral displacement is observed almost immediately after ARFI excitation transmission.

Table V summarizes all of the shear wave or lateral displacement wave velocities derived from presented data

TABLE V. Shear and lateral displacement wave velocities.

Source	Velocity (m/s)	r^2	Exp. No.
Optical axial	1.04 ± 0.02	0.99 ± 0.001	7[a]
FEM axial	1.04	1.00	7
Ultrasonically	1.07 ± 0.07	0.95 ± 0.02	8
Optical lateral	1.26 ± 0.25	0.98 ± 0.008	7[a]
FEM lateral	1.16	1.00	7
Boundary effect	0.97	0.99	1–4 and 6

[a]Only data from 2, 3, and −2 mm offsets used to ensure displacement estimates were not contained within the excitation volume.

sets. When possible, a mean and standard deviation (N=3) are offered. Shear wave speed estimates (i.e., wave speeds not derived from lateral displacements) yield good agreement, all with estimates around 1 m/s. The FEM modeling-derived ("FEM lateral") lateral displacement wave speed is significantly higher than any of the shear wave estimates, with a speed of 1.16 m/s. The mean optically derived ("optical lateral") lateral displacement wave speed is likewise higher than any mean shear wave speed. All wave velocity data, with mean $r^2 \geq 0.95$, are quite linear.

C. Proximal boundary effects

The effect of the proximal boundary (Exps. 1–4 and 6), which ranged from 3.3 to 4.8 mm from the imaging plane, was analyzed. Figure 8(a) presents a comparison of the time to peak PBSW reflection (axial) displacement for different proximal boundary distances. The plot illustrates that as the boundary gets progressively further away, the peak of the shear wave reflection it causes occurs later in time. This peak time and the propagation distance (which is approximately twice the boundary distance) share a direct, linear relationship, which is indicative of a constant shear wave velocity (0.97 m/s, Table V) in the medium. Figure 8(b) shows the dynamic response (axial displacement) of a single kernel, which was approximately 4.8 cm from the phantom's proximal boundary (Exp. 2). This plot demonstrates that the phantom completely recovers following the shear wave reflection artifact; an average of only 0.14 μm of residual displacement exists in the last 1.5 ms of plotted displacement.

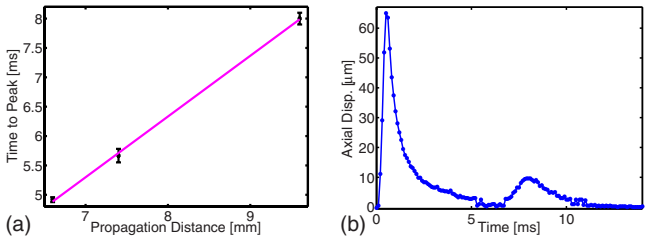

FIG. 8. (Color online) Proximal boundary effect comparison (a) and demonstration of phantom recovery (b). In the boundary effect plot, the mean and standard deviation (N=3) for time to the shear wave reflection peak for three proximal boundary distances [3.3 (Fig. 4), 3.7 ($CCoef_{worst}$ =[0.80,0.06,0.45]), and 4.8 mm ($CCoef_{worst}$=[0.85,0.03,0.58])] is plotted as a function of propagation distance (i.e., twice boundary distance). Linear regression fit (r^2=0.99) to means of these data is also plotted. In the recovery plot, the dynamic response of a single kernel is tracked until full recovery.

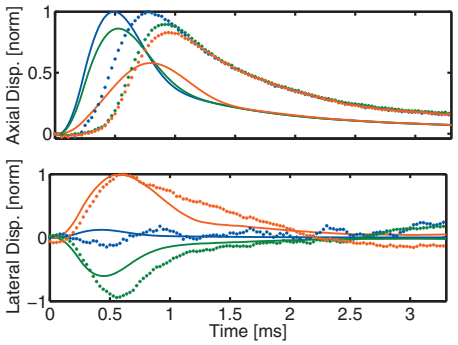

FIG. 9. Comparison of experimental (dots) and FEM (line) results for 0.2-ms, on-axis ARFI excitation. Axial (above) and lateral (below) displacement profiles are presented with normalized displacement scales. Trace coloring corresponds to kernel parameters listed in Table VI. Running average (167-μs kernel) was applied to all experimental lateral displacement data prior to plotting for FEM comparisons.

TABLE VI. On-axis FEM (Fig. 9) kernel parameters.

	Experimental results[a]		
Peak ax. disp. (norm)	1.00	0.90	0.83
Peak lat. disp. (norm)	−0.15[b]	−0.94	1.00
	FEM results		
Peak ax. disp. (norm)	1.00	0.86	0.58
Axial TTPD (ms)	0.49	0.53	0.80
Peak lat. disp. (norm)	0.12	−0.61	1.00
Lateral TTPD (ms)	0.43	0.45	0.58
Peak ax. velocity (m/s)	0.288	0.231	0.082
Velocity peak time (ms)	0.21	0.21	0.38
Trace color	B	G	R
Lateral pos. (mm)	0.04	−0.20	0.50
Axial pos. (mm)	−0.13	0.03	0.17

[a]TTPD values marked as bold in Table III.
[b]Search region limited to first 0.75 ms.

D. FEM modeling results

Figures 9 and 10 present a comparison of FEM modeling results and experimental tracking data. In the on-axis case, tracking data from Exp. 5 are compared to their matched FEM modeling result; in the off-axis case, FEM results are compared to data from Exp. 7 (1 and 2 mm offsets). Displacement traces are normalized to the peak value in their respective data set for all comparisons. For the regions and time frames analyzed, appreciable displacement was only observed in the simulation results through a depth range within ±1 cm of the transmit focus (i.e., 28–48 mm).

In the on-axis comparison (Fig. 9), there is reasonable agreement between peak normalized displacement values for both axial and lateral data. From the axial data (above), peak displacement and velocity decrease, while TTPD values increase with increasing kernel offset for both (i.e., FEM and experimental) data sets. Additionally, the leading edge of the displacement traces share a similar profile, which is consistent with peak velocities being of the same order and having percent differences all below 62%. There is a significant difference in TTPD values between data sets: displacement peaks in the simulated data occur much earlier than in the experimental data. If the blue traces are shifted to be coincident, however, percent differences between experimental and simulated TTPD values for the green and red traces are only 17% and 21%, respectively, if shifted by the same amount. Recovery profiles (i.e., portion of the trace following peak displacement) differ significantly between the two data sets, with the simulated data recovering noticeably faster than the experimental data.

The lateral displacement data (below in Fig. 9) share better agreement. Peak amplitudes and TTPD values increase with increasing kernel offset for both sets of results. Disregarding the nearly centered kernel (blue), which has displacement traces that are both quite flat, displacement is always directed away from the central axis in both tracking data. Much like the axial result, the leading edges of the displacement traces for the two more distal kernels exhibit a similar profile. Yet, unlike the axial result, the recovery profiles of these lateral data are fairly similar. The percent errors between TTPD values for the three kernels, in order of increasing kernel offset, are 9%, 22%, and 5%. On average for the three kernels, non-normalized, peak axial displacements are 142 times larger than non-normalized, peak lateral displacement magnitudes for the FEM data while they are only 29 times larger for the experimental data.

In the off-axis comparison (Fig. 10), agreement is quite good, particularly with the axial displacement data (above). Although recovery is still slower for the experimental data, the overall displacement profiles are quite similar between

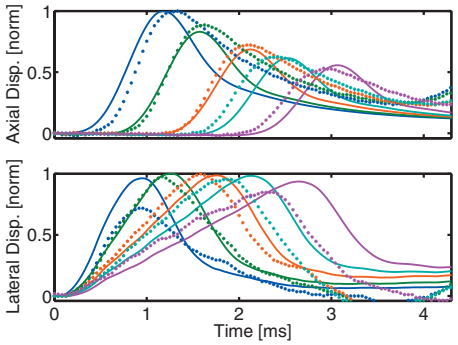

FIG. 10. Comparison of experimental (dots) and FEM (line) results for 0.4-ms, off-axis ARFI excitation. Axial (above) and lateral (below) displacement profiles presented with normalized displacement scales. Trace coloring corresponds to kernel parameters listed in Table VII.

TABLE VII. Off-axis FEM (Fig. 10) kernel parameters.

	Experimental results[a]				
Peak ax. disp. (norm)	1.00	0.89	0.72	0.63	0.53
Peak lat. disp. (norm)	0.72	0.98	1.00	0.95	0.85
	FEM results				
Peak ax. disp. (norm)	1.00	0.83	0.69	0.61	0.56
Axial TTPD (ms)	1.18	1.57	2.12	2.53	3.06
Peak lat. disp. (norm)	0.96	1.00	0.99	0.98	0.94
Lateral TTPD (ms)	0.95	1.27	1.76	2.13	2.65
Trace color	B	G	R	C	M
Lateral pos. (mm)	0.77	1.17	1.75	2.17	2.74
Axial pos. (mm)	−0.10	−0.05	0.01	−0.06	0.01

[a]TTPD values marked as bold in Table IV.

the two data sets. Unlike the on-axis data, experimental and FEM traces are relatively coincident, with TTPD value percent differences, in order of increasing kernel offset, of only 12%, 4%, 2%, 4%, and 5%. Normalized peak axial displacements shared similar agreement, with percent differences, in increasing offset order and excluding the normalization kernels of 7%, 4%, 2%, and 6%. In both data sets, as kernel offset increases, there is an increased delay before appreciable displacement is observed.

In the lateral displacement data comparison (below in Fig. 10), significant phenomena are observed. Both data sets present, independent of kernel offset, seemingly instantaneous and monotonically increasing displacement following ARFI excitation transmission. Additionally, with increasing kernel offset, peak displacement values begin increasing, reach an absolute peak (the normalization kernel), and then start decreasing in both data sets. Although TTPD values are not coincident, particularly at the two most distal kernels, they increase with increasing kernel offset in both the FEM and experimental cases. Percent differences, by increasing kernel offset, for TTPD values are 3%, 8%, 11%, 15%, and 13%, while percent differences in peak amplitude are 28%, 2%, 1%, 3%, and 10%. On average for the five kernels, non-normalized, peak axial displacements are 13 times larger than non-normalized, peak lateral displacements for both data sets.

IV. DISCUSSION

It was possible to accurately track embedded microspheres at depths nearing 5 mm, as evidenced by CCoef values typically above 0.85. Tracking reliability generally decreased (as indicated by reduced CCoef values) with increased FOV depth, as a result of increased optical scattering, and with increased frame rates, due to decreased SNR of the camera's sensor chip. The two greatest sources of experimental error were likely a result of inhomogeneity and registration issues. Inhomogeneities in the phantom material and/or beam intensity field accounted, in part, for discrepancies in observed dynamics between experiments or experimental trials. Temporally variant registration of a kernel and its corresponding microsphere or misregistration of the transducer/microscope foci resulted in inaccuracies in the estimation and spatial registration of induced displacements.

Material inhomogeneities in the phantom can arise during the production process or the experimental protocol itself. Given the inherent inhomogeneity of egg white solution, it is unlikely that a phantom with it as a principle base can be perfectly homogeneous. Such obviously inhomogeneous regions were specifically precluded from being experimental ROIs. In future experiments, the egg white solution will be filtered prior to its use in an attempt to further mitigate this effect. Material inhomogeneity can also result if egg white protein denatures due to heating generated from the microscope illumination source. In fact, it was for this very property that the basic phantom recipe was first employed by Takegami *et al.*[39] Although limiting illumination source use reduced this effect (with temperature increases $\leq 0.4\ ^{\circ}\mathrm{C}$ measured from illumination source heating alone), occasionally an ROI would become noticeably discolored as result of it, which required the designation of a new, neighboring ROI. Given the relatively short duration of the ARFI excitation pulses (≤ 0.4 ms) and the relatively long pulse repetition frequency (≥ 1 min), phantom heating due to absorption of acoustic radiation is thought to be insignificant. Using similar excitation pulses in a comparable medium, Palmeri *et al.*[45] estimated internal heating to be only a few tenths of a degree. Beam intensity "inhomogeneity" (i.e., deviation from the expected, axisymmetric transmission field of a circular piston) was either due to irregularities in the transmission path (as just discussed) or boundary condition artifacts. Reflections (of the longitudinal acoustic wave) at various interfaces (e.g., water/phantom or phantom/acrylic holder) could have resulted in significant aberration or attenuation of the acoustic intensity distribution at the ROI. Such focusing errors could have a substantial impact on the ARFI-induced response, as suggested by Eq. (3).

Registration issues accounted, in part, for inaccuracies in displacement characterization. As tracking CCoef values decreased, the registration between a microsphere and its corresponding kernel would worsen relative to the pre-excitation reference frame. Generally, this registration error manifested itself as tracking jitter while occasionally more significant displacement estimation inaccuracies resulted (e.g., the artifactual negative displacement in Fig. 5). Although the lowest CCoef values were achieved during transmission of the ARFI excitation (likely due to either in-plane motion blurring or significant out-of-plane motion of the microsphere), CCoef values were also noticeably affected by the camera sensor chip's SNR, which depended on framerate, sensitivity, and gain settings.

A second source of displacement characterization error originates from misregistration between the transducer and microscope foci. Given that the tip diameter of the needle hydrophone is on the same order as the push transducer's FWHM beamwidth, perfect lateral/elevational alignment is not possible. Additionally, elevational alignment of the hydrophone center with the microscope focal plane is not adequately achieved by merely ensuring that the needle tip is visibly in focus. This alignment technique can only ensure, assuming perfect elevational alignment between the hydrophone and push transducer foci, that the transducer's elevation focus is within a hydrophone tip radius (200 μm) of the microscope's imaging plane. Clear evidence of lateral misregistration is present in two of the data sets: the cyan kernel in Fig. 4 and the blue kernel in Fig. 7(a). In the first case, the cyan kernel peaked latest and achieved the greatest lateral displacement, despite not having the greatest reported lateral offset, suggesting that it was actually furthest from the excitation axis. In the second case, the sign of the blue kernel's lateral displacement is opposite the sign of its reported lateral position, implying that it moved *toward* the excitation center, which is physically implausible. Both inconsistencies are likely due to imperfect lateral registration between the FOV's and push transducer's lateral centers. Variation in axial position could have also introduced error in direct comparisons of different kernels. Yet, with the greatest range of axial positions in any data set only 340 μm, it is unlikely

that such error was significant given the much larger axial extent of the excitation beam.

Discrepancies between FEM modeling and experimental results are largely due to the misregistration and focusing issues detailed previously. In all FEM modeling results, the FOV lateral/elevational center was assumed to be perfectly coincident with the ARFI excitation lateral/elevational center. As already explained, such an assumption is not fully accurate. Thus, an improved characterization of a ROI's precise three-dimensional location would likely improve simulation agreement. Additionally, with broader excitation volumes generally resulting in a prolonged recovery period when compared to their narrower counterparts, differences in the effective beamwidth of the ARFI excitation would account, in part, for the discrepancy in recovery profiles observed between FEM and experimental axial displacement data.[24] The extended recovery phase in the experimental data might also have been influenced by boundary conditions (e.g., the proximal boundary) not properly accounted for in the FEM model. Additionally, the viscoelastic nature of the phantom—as opposed to the purely elastic behavior assumed in the model—could have influenced dynamics, particularly for those observed in the recovery profile. Thus, inclusion of viscosity into the FEM model could also improve agreement in the future.

The off-axis tracking data offered perhaps the most interesting findings. In the lateral displacement data, the seemingly instant displacement observed in all off-axis, lateral displacement plots [Figs. 7(b)–7(d) and below in Fig. 10] is likely due to a Poisson effect, which requires instant, global redistribution of an incompressible medium when a local strain field is applied to it. An ARFI excitation causes mass within its beam volume to displace away from the push transducer, with preferential force applied (resulting in increased displacement) to mass located near the beam's focus. When this focal volume displaces away from the transducer, surrounding phantom material must redistribute due to its nearly incompressible nature. Material deep to the focus must displace away from the central beam axis to "make room" for the newly displaced volume while material shallow to the focus must displace toward the beam axis to "fill in" for this volume. Given that the phantom was not perfectly incompressible, this redistribution does not happen instantaneously but rather at a speed which is orders of magnitude faster than the shear wave velocity.

In the off-axis, axial displacement data [Figs. 6(b)–6(d)], the progressive dispersion and attenuation observed in PBSW reflection TTPD and peak displacement values, respectively, are due to the increasing shear wave propagation distance to more distal kernels. If the shear wave reflection is thought to have emanated from the excitation's image across the proximal boundary (so hypothetically near the microscope's objective), it becomes clear that reflected wave propagation distances will be least for kernels nearest the axis connecting the source/image foci. As kernels are positioned further from this axis, reflected shear wave propagation distances increase, which results in later TTPD values and greater peak attenuations at those times.

In the future, it is hoped that significant improvements can be made in design of the optical phantom. To increase the number of trackable microspheres within the FOV, a highly populated "monolayer" of microspheres can be generated in the phantom at a specific depth from the proximal boundary. This can be achieved by superficially applying a layer of microspheres on the phantom's original proximal boundary then casting a thin, matched layer atop the microspheres to form a new proximal boundary; this is a similar concept to the dual-stage casting technique employed by Andreev *et al.*[31] This multi-staged fabrication process can then be taken a step further by adding a third, minimally scattering (optically), mechanically matched layer atop the second layer in an attempt to increase the effective proximal boundary distance without drastically compromising microscope imaging quality. A gelatin layer without egg white or microspheres could be nearly transparent (which would increase light transmission and improve focusing ability) and formulated to match the stiffness of the other two layers, which would eliminate (or severely mitigate) the creation of a shear wave reflection at that boundary and would extend the PBSW reflection distance to the more distal boundary of this third layer.

It is also the authors' intention to construct mechanically inhomogeneous optical phantoms for the purpose of investigating shear wave dynamics at material interfaces. If these second and third layers were cast from a higher bloom strength gelatin (or if two different gelatin phases were created in the transverse plane, in alignment with the microscope axis), there would be an appreciable mechanical contrast at this interface. It would then be possible to investigate (optically) how a shear wave propagates along or couples into such a boundary. With regard to the experimental setup, improvements to the transducer micro-positioning system could be made to allow for closer (relative to the microscope's FOV) transducer placement; this would facilitate optical investigation of the dynamic response shallow to the excitation focus. Additionally, the push transducer, or an added opposing but coaxial "tracking" transducer, could be utilized for the purpose of synchronized and matched ultrasonically based tracking of the post-ARFI response, similar to the approach implemented previously by Bouchard *et al.*[36]

Despite the inhomogeneity and registration issues addressed herein, the presented optically based method is capable of accurately tracking, with improved spatial and temporal resolutions, the dynamic response of a tissue-mimicking phantom at depth. Although the phantom's proximal boundary introduces a clear artifact later in time, its influence is predictable [Fig. 8(a)] and does not appear to affect the final recovery of the phantom [Fig. 8(b)]. Post-excitation, axial displacement results from similar FEM models have previously been validated with experimental data obtained in a semi-infinite phantom environment.[16] Thus, corroboration of experimentally observed dynamical phenomena and displacement trace morphologies with FEM results suggest that the optical phantom setup, early in time, is able to facilitate similar ARFI-induced dynamics as those generated in a semi-infinite medium. Additionally, independent experimental validation of optical tracking is offered

through ultrasonically based shear wave velocimetry (Exp. 8), which yielded a velocity estimate that is not statistically differentiable from the one provided by the optically based technique.

V. CONCLUSION

Optical tracking of ARFI-induced dynamics in a tissue-mimicking phantom was successfully achieved at frame rates of up to 36 kHz and with sub-micron displacement resolution in the axial and lateral dimensions. These tracking data show good agreement with all basic trends and phenomena observed in matched FEM modeling results early in time (up to 4 ms). Excellent agreement is also observed between shear wave velocities derived from the optical technique and those yielded by an independent ultrasonically based method. Due to the closeness of the phantom's proximal boundary, an artifact-generating shear wave reflection was observed in all data sets later in time (around 5 ms in most cases shown). It is hoped that this artifact as well as the limited number of tracking kernels available within a FOV can be addressed in the future with an improved phantom design. Despite the restricted clinical applicability of this tracking technique, it could assist in gaining a greater understanding of complex radiation force dynamics in tissue-mimicking phantoms.

ACKNOWLEDGMENTS

This work was supported in part by a National Science Foundation Graduate Research Fellowship. The authors thank Gijs van Soest, Carl Herickhoff, and Michael Giacomelli for their insight and Ned Rouze for intensity measurement assistance.

[1]K. R. Nightingale, M. L. Palmeri, R. W. Nightingale, and G. E. Trahey, "On the feasibility of remote palpation using acoustic radiation force," J. Acoust. Soc. Am. **110**, 625–634 (2001).
[2]D. Melodelima, J. Bamber, F. Duck, J. Shipley, and L. Xu, "Elastography for breast cancer diagnosis using radiation force: System development and performance evaluation," Ultrasound Med. Biol. **32**, 387–396 (2006).
[3]Y. A. Ilinskii, G. D. Meegan, E. A. Zabolotskaya, and S. Y. Emelianov, "Gas bubble and solid sphere motion in elastic media in response to acoustic radiation force," J. Acoust. Soc. Am. **117**, 2338–2346 (2005).
[4]R. H. Behler, T. C. Nichols, H. Zhu, E. P. Merricks, and C. M. Gallippi, "ARFI imaging for noninvasive material characterization of atherosclerosis Part II: Toward *in vivo* characterization," Ultrasound Med. Biol. **35**, 278–295 (2009).
[5]J. Bercoff, M. Tanter, and M. Fink, "Supersonic shear imaging: A new technique for soft tissue elasticity mapping," IEEE Trans. Ultrason. Ferroelectr. Freq. Control **51**, 396–409 (2004).
[6]A. Sarvazyan, O. Rudenko, S. Swanson, J. Fowlkes, and S. Emelianov, "Shear wave elasticity imaging: A new ultrasonic technology of medical diagnostics," Ultrasound Med. Biol. **24**, 1419–1435 (1998).
[7]S. A. McAleavey, M. Menon, and J. Orszulak, "Shear-modulus estimation by application of spatially-modulated impulsive acoustic radiation force," Ultrason. Imaging **2**, 87–104 (2007).
[8]E. E. Konofagou and K. Hynynen, "Localized harmonic motion imaging: Theory, simulations and experiments," Ultrasound Med. Biol. **29**, 1405–1413 (2003).
[9]M. Fatemi and J. F. Greenleaf, "Vibro-acoustography: An imaging modality based on ultrasound-stimulated acoustic emission," Proc. Natl. Acad. Sci. U.S.A. **96**, 6603–6608 (1999).
[10]F. Viola and W. F. Walker, "Radiation force imaging of viscoelastic properties with reduced artifacts," IEEE Trans. Ultrason. Ferroelectr. Freq. Control **50**, 736–742 (2003).
[11]J. Ophir, I. Céspedes, H. Ponnekanti, Y. Yazdi, and X. Li, "Elastography: A quantitative method for imaging the elasticity of biological tissues," Ultrason. Imaging **13**, 111–134 (1991).
[12]K. Hoyt, T. Kneezel, B. Castaneda, and K. J. Parker, "Quantitative sonoelastography for the *in vivo* assessment of skeletal muscle viscoelasticity," Phys. Med. Biol. **53**, 4063–4080 (2008).
[13]S. J. Hsu, R. R. Bouchard, D. M. Dumont, P. D. Wolf, and G. E. Trahey, "*In vivo* assessment of myocardial stiffness with acoustic radiation force impulse imaging," Ultrasound Med. Biol. **33**, 1706–1719 (2007).
[14]J. L. Gennisson, S. Catheline, S. Chaffaï, and M. Fink, "Transient elastography in anisotropic medium: Application to the measurement of slow and fast shear wave speeds in muscles," J. Acoust. Soc. Am. **114**, 536–541 (2003).
[15]H. Kanai, "Propagation of spontaneously actuated pulsive vibration in human heart wall in *in vivo* viscoelasticity estimation," IEEE Trans. Ultrason. Ferroelectr. Freq. Control **52**, 1931–1942 (2005).
[16]M. L. Palmeri, A. C. Sharma, R. R. Bouchard, R. W. Nightingale, and K. R. Nightingale, "A finite-element method model of soft tissue response to impulsive acoustic radiation force," IEEE Trans. Ultrason. Ferroelectr. Freq. Control **52**, 1699–1712 (2005).
[17]P. J. Westervelt, "The theory of steady forces caused by sound waves," J. Acoust. Soc. Am. **23**, 312–315 (1951).
[18]M. E. Lyons and K. J. Parker, "Absorption and attenuation in soft tissues. II. Experimental results," IEEE Trans. Ultrason. Ferroelectr. Freq. Control **35**, 511–521 (1988).
[19]W. Nyborg, "Acoustic streaming," in *Physical Acoustics*, edited by W. Mason (Academic, New York, 1965), Vol. **IIB**, Chap. 11, pp. 265–331.
[20]G. R. Torr, "The acoustic radiation force," Am. J. Phys. **52**, 402–408 (1984).
[21]W. Lai, D. Rubin, and E. Krempl, *Introduction to Continuum Mechanics* (Butterworth-Heinemann, Woburn, MA, 1999).
[22]J. Bishop, G. Poole, and D. Plewes, "Magnetic resonance imaging of shear wave propagation in excised tissue," J. Magn. Reson. Imaging **8**, 1257–1265 (1998).
[23]M. Fatemi and J. F. Greenleaf, *Topics in Applied Physics* (Springer Berlin, Heidelberg, 2002), Vol. **84**, pp. 257–276.
[24]M. L. Palmeri, S. A. McAleavey, K. L. Fong, G. E. Trahey, and K. R. Nightingale, "Dynamic mechanical response of elastic spherical inclusions to impulse acoustic radiation force excitation," IEEE Trans. Ultrason. Ferroelectr. Freq. Control **53**, 2065–2079 (2006).
[25]G. F. Pinton, J. J. Dahl, and G. E. Trahey, "Rapid tracking of small displacements with ultrasound," IEEE Trans. Ultrason. Ferroelectr. Freq. Control **53**, 1103–1117 (2006).
[26]M. A. Lubinski, S. Y. Emelianov, K. R. Raghavan, A. E. Yagle, A. R. Skovoroda, and M. O'Donnell, "Lateral displacement estimation using tissue incompressibility," IEEE Trans. Ultrason. Ferroelectr. Freq. Control **43**, 247–256 (1996).
[27]R. R. Bouchard, J. J. Dahl, S. J. Hsu, M. L. Palmeri, and G. E. Trahey, "Image quality, tissue heating, and frame rate trade-offs in acoustic radiation force impulse imaging," IEEE Trans. Ultrason. Ferroelectr. Freq. Control **56**, 63–76 (2009).
[28]C. Maleke, M. Pernot, and E. E. Konofagou, "Single-element focused ultrasound transducer method for harmonic motion imaging," Ultrason. Imaging **28**, 144–158 (2006).
[29]M. L. Palmeri, S. A. McAleavey, G. E. Trahey, and K. R. Nightingale, "Ultrasonic tracking of acoustic radiation force-induced displacements in homogeneous media," IEEE Trans. Ultrason. Ferroelectr. Freq. Control **53**, 1300–1313 (2006).
[30]J. Schmitt, "OCT elastography: Imaging microscopic deformation and strain of tissue," Opt. Express **3**, 199–211 (1998).
[31]V. G. Andreev, V. N. Dmitriev, Y. A. Pischal'nikov, O. V. Rudenko, O. A. Sapozhnikov, and A. P. Sarvazyan, "Observation of shear waves excited by focused ultrasound in a rubber-like media," Acoust. Phys. **43**, 123–128 (1996).
[32]E. Bossy, A. R. Funke, K. Daoudi, A.-C. Boccara, M. Tanter, and M. Fink, "Transient optoelastography in optically diffusive media," Appl. Phys. Lett. **90**, 174111 (2007).
[33]P. A. Dayton, K. E. Morgan, A. L. Klibanov, G. Brandenburger, K. R. Nightingale, and K. W. Ferrara, "A preliminary evaluation of the effects of primary and secondary radiation forces on acoustic contrast agents," IEEE Trans. Ultrason. Ferroelectr. Freq. Control **44**, 1264–1277 (1997).
[34]P. Palanchon, P. Tortoli, A. Bouakaz, M. Versluis, and N. de Jong, "Optical observation of acoustical radiation force effects on individual air bubbles," IEEE Trans. Ultrason. Ferroelectr. Freq. Control **52**, 104–110 (2005).
[35]P. A. Dayton, J. S. Allen, and K. W. Ferrara, "The magnitude of radiation force on ultrasound contrast agents," J. Acoust. Soc. Am. **112**, 2183–2192

(2002).
[36]R. R. Bouchard, G. van Soest, G. E. Trahey, and A. F. W. van der Steen, "Optical tracking of superficial dynamics from an acoustic radiation force-induced excitation," Ultrason. Imaging **31**, 17–30 (2009).
[37]M. C. W. van Rossum and T. M. Nieuwenhuizen, "Multiple scattering of classical waves: Microscopy, mesoscopy, and diffusion," Rev. Mod. Phys. **71**, 313–371 (1999).
[38]P. Sheng, *Introduction to Wave Scattering, Localization, and Mesoscopic Phenomena* (Academic, New York, 1995).
[39]K. Takegami, Y. Kaneko, T. Watanabe, T. Maruyama, Y. Matsumoto, and H. Nagawa, "Polyacrylamide gel containing egg white as new model for irradiation experiments using focused ultrasound," Ultrasound Med. Biol. **30**, 1419–1422 (2004).
[40]T. J. Hall, M. Bilgen, M. F. Insana, and T. A. Krouskop, "Phantom materials for elastography," IEEE Trans. Ultrason. Ferroelectr. Freq. Control **44**, 1355–1365 (1997).
[41]F. W. Kremkau, R. W. Barnes, and P. McGraw, "Ultrasonic attenuation and propagation speed in normal human brain," J. Acoust. Soc. Am. **70**, 29–38 (1981).
[42]M. L. Palmeri, M. H. Wang, J. J. Dahl, K. D. Frinkley, and K. R. Nightingale, "Quantifying hepatic shear modulus *in vivo* using acoustic radiation force," Ultrasound Med. Biol. **34**, 546–558 (2008).
[43]J. A. Jensen and N. B. Svendsen, "Calculation of pressure fields from arbitrarily shaped, apodized, and excited ultrasound transducers," IEEE Trans. Ultrason. Ferroelectr. Freq. Control **39**, 262–267 (1992).
[44]J. A. Jensen, "Field: A program for simulating ultrasound systems," in Proceedings of the 10th Nordic-Baltic Conference on Biomedical Imaging (1996), Vol. **34**, pp. 351–353.
[45]M. Palmeri and K. Nightingale, "On the thermal effects associated with radiation force imaging of soft tissue," IEEE Trans. Ultrason. Ferroelectr. Freq. Control **51**, 551–565 (2004).